

# Constructing Polymorphic Nanodomains in BaTiO<sub>3</sub> Films via Epitaxial Symmetry Engineering

Wei Peng, Jacob A. Zorn, Junsik Mun, Muhammad Sheeraz, Chang Jae Roh, Jun Pan, Bo Wang, Kun Guo, Chang Won Ahn, Yaping Zhang, Kui Yao, Jong Seok Lee, Jin-Seok Chung, Tae Heon Kim, Long-Qing Chen, Miyoung Kim, Lingfei Wang,\* and Tae Won Noh\*

Ferroelectric materials owning a polymorphic nanodomain structure usually exhibit colossal susceptibilities to external mechanical, electrical, and thermal stimuli, thus holding huge potential for relevant applications. Despite the success of traditional strategies by means of complex composition design, alternative simple methods such as strain engineering have been intensively sought to achieve a polymorphic nanodomain state in lead-free, simple-composition ferroelectric oxides in recent years. Here, a nanodomain configuration with morphed structural phases is realized in an epitaxial BaTiO<sub>3</sub> film grown on a (111)-oriented SrTiO<sub>3</sub> substrate. Using a combination of experimental and theoretical approaches, it is revealed that a threefold rotational symmetry element enforced by the epitaxial constraint along the [111] direction of BaTiO<sub>3</sub> introduces considerable instability among intrinsic tetragonal, orthorhombic, and rhombohedral phases. Such phase degeneracy induces ultrafine ferroelectric nanodomains (1–10 nm) with low-angle domain walls, which exhibit significantly enhanced dielectric and piezoelectric responses compared to the (001)-oriented BaTiO<sub>3</sub> film with uniaxial ferroelectricity. Therefore, the finding highlights the important role of epitaxial symmetry in domain engineering of oxide ferroelectrics and facilitates the development of dielectric capacitors and piezoelectric devices.

## 1. Introduction

Realizing structure/phase degeneracy in solids has proven crucial in modern functional material design.<sup>[1–3]</sup> A prominent example is the so-called morphotropic phase boundary (MPB) in ferroelectric materials.<sup>[4–6]</sup> The energy degeneracy of different polar structures with varying symmetries at the phase boundary gives rise to significant reduction of polarization anisotropy as well as domain wall energy, which further bring about the formation of nanodomains.<sup>[7–10]</sup> In such a polymorphic nanodomain state, the polarization is subject to rotation under external fields, thus yielding large response.<sup>[6,11,12]</sup> Significant success has been achieved via complex composition engineering in oxide solid solutions to design ferroelectric MPB in earlier times. Inspired by the rapid advancements in heteroepitaxy techniques, recent efforts have been devoted to

Dr. W. Peng, Prof. L. Wang, Prof. T. W. Noh  
Center for Correlated Electron Systems  
Institute for Basic Science  
Seoul 08826, Republic of Korea  
E-mail: lingfei.wang@snu.ac.kr; twnoh@snu.ac.kr

Dr. W. Peng, Prof. L. Wang, Prof. T. W. Noh  
Department of Physics and Astronomy  
Seoul National University  
Seoul 08826, Republic of Korea

J. A. Zorn, B. Wang, Prof. L.-Q. Chen  
Department of Materials Science and Engineering  
Pennsylvania State University  
University Park, PA 16802, USA

J. Mun, Prof. M. Kim  
Department of Materials Science and Engineering  
and Research Institute of Advanced Materials  
Seoul National University  
Seoul 08826, Republic of Korea

M. Sheeraz, Prof. C. W. Ahn, Prof. T. H. Kim  
Department of Physics and Energy Harvest-Storage  
Research Center (EHSRC)  
University of Ulsan  
Ulsan 44610, Republic of Korea

C. J. Roh, Prof. J. S. Lee  
Department of Physics and Photon Science  
Gwangju Institute of Science and Technology  
Gwangju 61005, Republic of Korea

Dr. J. Pan  
College of Materials Science and Engineering  
Zhejiang University of Technology  
Hangzhou 310014, P. R. China

K. Guo, Prof. K. Yao  
Institute of Materials Research and Engineering  
A\*STAR (Agency for Science, Technology and Research)  
Singapore 138634, Singapore

Dr. Y. Zhang  
Imaging and Characterization Core Lab  
King Abdullah University of Science and Technology  
Thuwal 23955-6900, Kingdom of Saudi Arabia

Prof. J.-S. Chung  
Department of Physics  
Soongsil University  
Seoul 06978, Republic of Korea

 The ORCID identification number(s) for the author(s) of this article can be found under <https://doi.org/10.1002/adfm.201910569>.

DOI: 10.1002/adfm.201910569

seeking alternative simple methods to achieve a similar polymorphic or energy-degenerated nanodomain state in epitaxial ferroelectric oxide thin films.<sup>[4,13–15]</sup> One of the most important and successful strategy is strain engineering. For example, it was reported that appropriate epitaxial strain can position BiFeO<sub>3</sub> films on a boundary between rhombohedral and tetragonal phases.<sup>[4]</sup> Such a strain-driven MPB-like domain structure leads to a promising electromechanical response of the epitaxial BiFeO<sub>3</sub> film. However, reports of similar material systems are still scarce to date.

Despite the success of traditional strain engineering in designing crystalline structures and manipulating properties of epitaxial heterostructures, there are several restrictions impeding its further advancement.<sup>[16]</sup> For example, the strategy can be only effective in relatively thin films (usually several to tens of nanometers) that can maintain a coherently strained state, rendering as-designed heterostructures unsuitable for high-voltage applications. The magnitude of strain that an epitaxial film can endure is also relatively small (typically 1–2%). In addition, the limited number of commercial substrates poses a lack of continuous strain tunability.

The epitaxial orientation, as an alternative control parameter in heterostructure customization, has recently attracted rising interests for ferroelectric phase and domain design.<sup>[17–19]</sup> Several studies have revealed that the (111) orientation of a cubic substrate can introduce new types of phase instability and structure competition in a tetragonal ferroelectric via a dissimilar surface symmetry element, which we term epitaxial symmetry engineering. For example, unlike the commonly observed tetragonal phase in (001)-oriented PbTiO<sub>3</sub> film, a SrTiO<sub>3</sub> (111) substrate tends to drive the polarization of overlaid PbTiO<sub>3</sub> toward the cube diagonal, thus giving rise to a new monoclinic phase.<sup>[17]</sup> This is a consequence of the epitaxial constraint with a threefold rotational symmetry around the [111] direction of the cubic substrate. By the same token, lamellar twinned nanodomain (around 40 nm) structures composed of three tetragonal variants can form in (111)-oriented PbZr<sub>0.2</sub>Ti<sub>0.8</sub>O<sub>3</sub> films.<sup>[18]</sup> The complex domain structures contain rich elastic and electrostatic interactions, leading to unusual ferroelastic domain switching.<sup>[19]</sup> However, these reported ferroelectric systems via epitaxial symmetry engineering contain only single structural phase, which poses restriction for accessible polarization directions. This restriction then substantially limits the freedom of polarization rotation, thus suppressing field-driven responses.

BaTiO<sub>3</sub> (BTO) is a tetragonal ferroelectric at room temperature and shows consecutive transition to orthorhombic (at ≈300 K) and then rhombohedral (at ≈190 K) polar phases upon cooling.<sup>[20]</sup> The availability of such abundant phases in a temperature range of 100 K (corresponding to an energy scale of 0.009 eV) hints the possibility of constructing a polymorphic domain system in BaTiO<sub>3</sub> epitaxial films by exploiting rich local interactions in a multidomain system. Despite the great promise, successful achievement of nanodomains with coexistent orthorhombic-like and tetragonal-like structures has been only reported recently in BTO films grown on an orthorhombic GdScO<sub>3</sub> (110) substrate by utilizing the anisotropic misfit strain.<sup>[21,22]</sup> Moreover, the study of the polymorphic nanodomain structure in BTO films, especially from the perspective of microstructure-function relationship, has not been well established.

In this report, we demonstrate a new polymorphic nanodomain state in strain-relaxed BTO films (with a thickness of ten to hundreds of nanometers) epitaxially grown on SrTiO<sub>3</sub> (111) substrates with an intermediate SrRuO<sub>3</sub> layer [henceforth (111)-BTO]. Using scanning transmission electron microscopy (STEM), we show the state consists of ultrafine domains with their sizes ranging from 1 to 10 nm, and coexisting rhombohedral, orthorhombic, and tetragonal structures. Notably, this domain structure is far more complex than other polymorphic domain systems discovered previously in simple oxide ferroelectrics such as BiFeO<sub>3</sub>, but surprisingly resembles the slush-like polar nanoregions of conventional relaxor ferroelectrics.<sup>[23]</sup> However, unlike relaxor ferroelectrics that require chemical inhomogeneity to produce polar nanoregions, the domain structure in (111)-BTO is a result of the mechanical clamping from a cubic substrate with a threefold rotational symmetry element according to phase field simulations. Furthermore, the particular domain structure leads to several relaxor-like features such as strong polarization relaxation and frequency-dispersive dielectric peaks, which have not been reported in previous polymorphic nanodomain systems of simple oxide ferroelectrics. As a consequence, (111)-BTO exhibits significantly enhanced dielectric and piezoelectric response, compared to its (001) counterpart [namely (001)-BTO]. Therefore, compared to previous works of (111)-oriented ferroelectrics, our study further reveals the huge potential of epitaxial symmetry engineering by demonstrating successful construction of complex domain structures with intriguing functional properties as those of conventional relaxor ferroelectrics.

## 2. Results and Discussion

We focus our study on 330 nm thick, high-quality epitaxial BTO films on both STO (001) and (111) substrates with an intermediate SrRuO<sub>3</sub> (SRO) electrode layer by pulsed laser deposition (PLD) (see the Experimental Section). The excellent epitaxial qualities of these heterostructures were verified by atomic force microscopy and X-ray diffraction (Figures S1–S5, Supporting Information). It is worth noting that the misfit strain was fully relaxed in both thick films. Especially, (111)-BTO has a rather small critical thickness (several nanometers) for strain relaxation (Figure S4, Supporting Information), resulting in similar properties in a broad thickness range (from ten to hundreds of nanometers). Therefore, the epitaxial symmetry plays a dominant role in the interplay between the mechanical constraint and ferroelectric domain formation in the (111) case. More specifically, the cubic STO substrate can enforce a threefold rotational symmetry element along the out-of-plane [111] direction of BTO via macroscale mechanical clamping. Such an emergent symmetry element in BTO will introduce rich elastic and electrostatic interactions among the inherent tetragonal domains at room temperature, thus inducing significant structure instabilities with the emergence of novel domain structures.

We first investigated the ferroelectric properties of the (001)- and (111)-BTO films using a Pt/SRO/BTO/SRO/STO capacitor structure (Figure 1a). Both structures have negligible leakage current under electric biases higher than 10 V

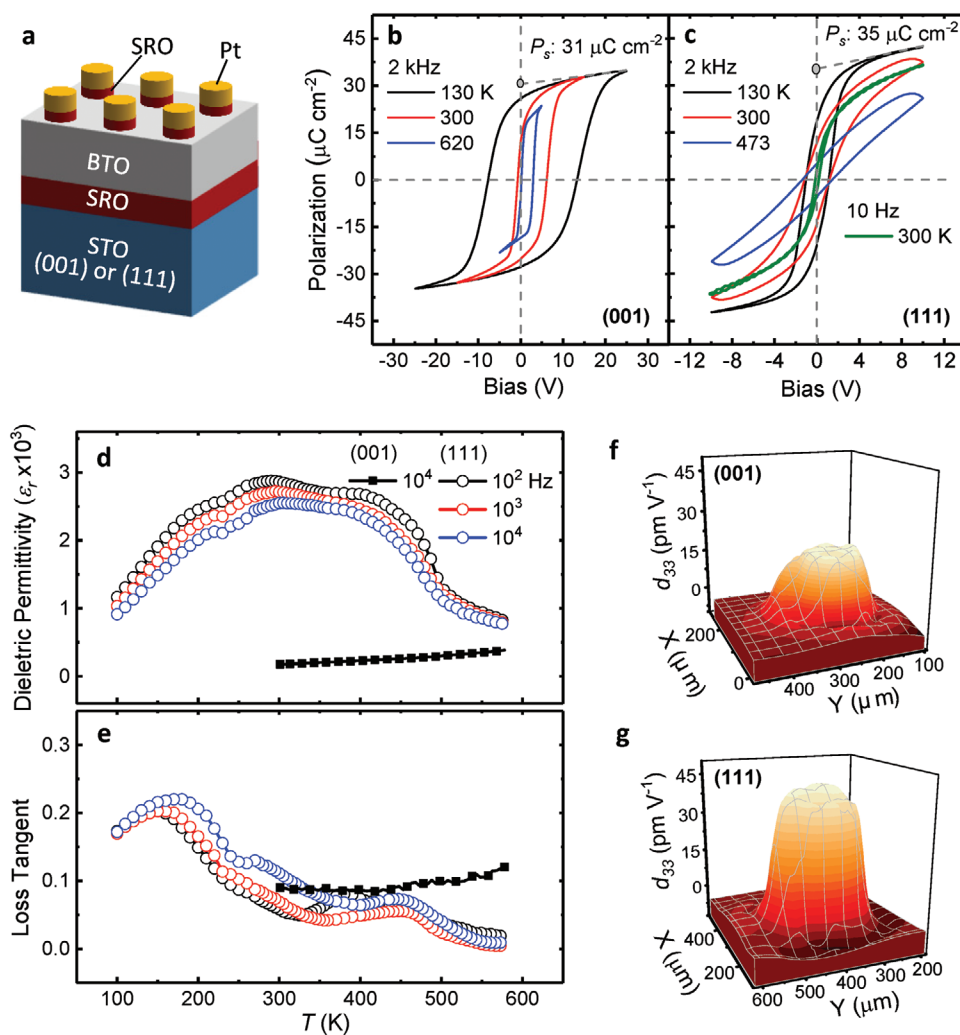


**Figure 1.** a) Schematic of the electrical measurement device. b,c) Temperature-dependent  $P$ - $E$  hysteresis loops of b) (001)-BTO and c) (111)-BTO measured at 2 kHz. For (111)-BTO, the hysteresis loop measured at 300 K with a frequency of 10 Hz is also shown. The saturated polarization ( $P_s$ ) of (001)- and (111)-BTO at 130 K are labeled for comparison. d,e) Temperature-dependent dielectric permittivity (d) and dielectric loss (e) of (111)-BTO measured with varying probing frequencies. The dielectric permittivity and dielectric loss of (001)-BTO measured at  $10^4$  Hz are shown for comparison. f,g) The effective  $d_{33}$  of (001)-f) and (111)-BTO g), measured on the capacitor structure shown in (a) by LSV.

(Figure S6, Supporting Information). In marked contrast to the square-like polarization-electric field ( $P$ - $E$ ) hysteresis loop of (001)-BTO (Figure 1b), (111)-BTO exhibits a slim hysteresis loop at room temperature with probing frequencies of 10 and 2000 Hz (Figure 1c), suggesting strong polarization relaxation. The different polarization behaviors were also confirmed by piezoelectric force microscopy (PFM, Figure S8, Supporting Information). Moreover, the square-like  $P$ - $E$  loop of (111)-BTO at 130 K indicates that the relaxation is significantly suppressed at low temperatures (Figure 1c). The temperature-dependent polarization relaxation is reminiscent of relaxor ferroelectricity,<sup>[24]</sup> and may suggest a metastable polar domain state in (111)-BTO, which is subject to the competition among local fields, epitaxial constraint, and thermal fluctuation. From a functional point of view, the diminishing hysteresis and remnant polarization along with large saturated polarization render (111)-BTO particularly promising for efficient, high-density dielectric capacitors.<sup>[25]</sup>

Analysis of the temperature-dependent dielectric permittivity of (111)-BTO with varying probing frequencies can provide insights into the polarization relaxation dynamics and hints about possible phase transitions (Figure 1d,e). One important feature of (111)-BTO is its large dielectric permittivity, with a value of over 1000 spanning a broad temperature range for probing frequencies up to  $10^4$  Hz. This value is an order of magnitude larger than those of other conventional ferroelectric films, such as (001)-BTO (Figure 1d and Figure S7, Supporting Information), and even some relaxor ferroelectric thin films.<sup>[25–27]</sup> Another noticeable feature is the existence of frequency-dispersive peaks in the temperature range of 250–350 K. As the probing frequency decreases, the temperature of the local dielectric permittivity maximum shifts to a lower value. This type of dielectric relaxation has been widely observed in relaxor ferroelectrics as well as ferroelectric MPB systems, which has been usually ascribed to the different dielectric response of nanodomains under

varying local circumstances, rather than a macroscopic phase transition.<sup>[28–30]</sup>

Two additional broad dielectric anomalies centered at  $\approx 400$  and  $200$  K can be also identified in the dielectric spectra of (111)-BTO. The negligible frequency dispersion of their peak temperatures suggests a nature of diffusive phase transition. The higher-temperature anomaly should correspond to a ferroelectric-paraelectric phase transition, which is supported by the nearly linear  $P$ - $E$  loop at  $473$  K, resembling that of a paraelectric phase (Figure 1c). The maximum temperature of the anomaly, i.e.,  $\approx 400$  K, is close to the Curie temperature of bulk BTO, as expected for a strain-relaxed BTO film. The lower-temperature anomaly should correspond to a transition event between two ferroelectric phases, which we analyze based on structure study in more detail below.

Another intriguing figure of merit for (111)-BTO is its considerably enhanced piezoresponse compared to (001)-BTO. The piezoresponse of BTO films under the substrate clamping condition was measured by a laser scanning vibrometer (LSV), which provides a reliable analysis by directly detecting the macroscale surface displacement of the top electrode under a driven bias.<sup>[31]</sup> As shown in Figure 1f,g, (111)-BTO exhibits an effective  $d_{33}$  value of  $48 \text{ pm V}^{-1}$ , increasing by more than 100% over  $20 \text{ pm V}^{-1}$  of (001)-BTO. This enhancement may again point to a particular domain structure in (111)-BTO in contrast to the uniaxial ferroelectric system of (001)-BTO.

To understand the extraordinary dielectric and piezoelectric properties of (111)-BTO, as well as its particular dielectric behavior, we carried out a comprehensive structure study. A macroscopic threefold rotational symmetry element around the out-of-plane [111] direction was first revealed by the second harmonic generation (SHG) measurement (Figure 2a and Figure S9, Supporting Information). The measured SHG signal was best fit with a rhombohedra symmetry ( $C_{3v}$ ) model. The threefold rotational symmetry was verified by asymmetric reciprocal space mapping (RSM) via X-ray diffraction (Figure S4, Supporting Information).

Raman spectroscopy revealed microscale structural fingerprints. As shown in Figure 2b, (111)-BTO shows the typical Raman modes of a tetragonal phase of BTO [ $A_1(\text{TO}_3)$ ,  $A_1(\text{LO}_3)$ ,  $A_1(\text{TO}_2)$ ,  $E(\text{LO}_2)$ , and  $E(\text{TO}_3)$ ].<sup>[32]</sup> Moreover, the presence of a smearing  $E(\text{LO}_2+\text{TO}_3)$  mode and an  $A_1(\text{TO}_1)$  mode suggests coexistence of rhombohedra and/or orthorhombic phases.<sup>[33]</sup> It is worth noting that neither a tetragonal nor an orthorhombic structure owns a threefold rotational symmetry element along the [111] direction. This inconsistency between the macroscopic and microscopic structural symmetry can only be explained by reference to a microscopic scenario based on nanodomains: three equivalent tetragonal and orthorhombic variants exist in the form of nanodomains but occupy equal volumes on a macro scale, as enforced by the cubic substrate symmetry; this picture is similar as those macroscopic high-symmetry phases detected in canonical relaxor ferroelectrics and ferroelectric solid solutions with nanodomains.<sup>[34,35]</sup> In addition, the Raman spectra at  $475$  and  $525$  K with diminishing polar mode intensity confirms the existence of a ferroelectric-paraelectric phase transition on the high temperature side. Furthermore, a possible transition to a dominant rhombohedral phase at low temperatures can be inferred from the redshift of the  $A_1(\text{TO}_2)$  mode and the blueshift of the  $A_1(\text{TO}_3)$  mode with decreasing temperature.<sup>[36]</sup>

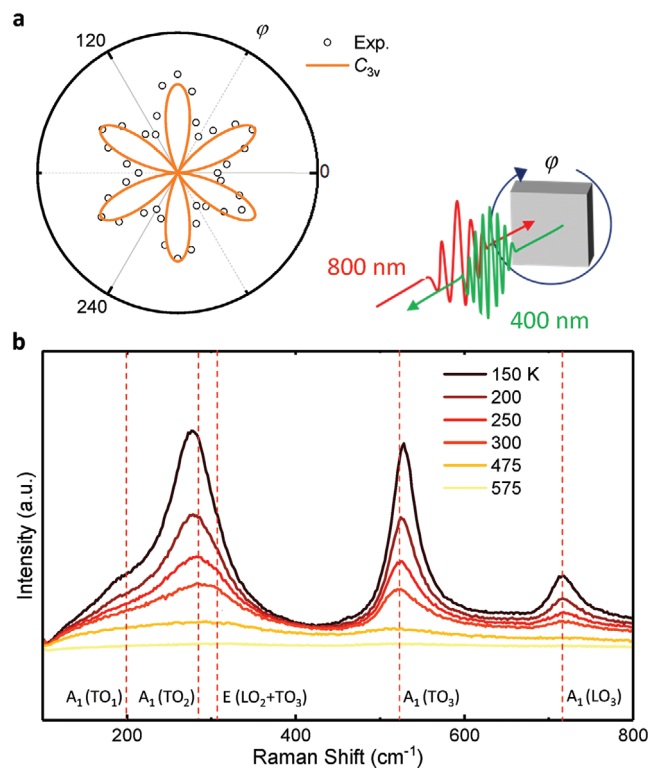


**Figure 2.** a) Azimuth-dependent SHG signal intensity of (111)-BTO. A best fitting of the experimental data with respect to the rhombohedral symmetry ( $C_{3v}$ ) model is shown, suggesting a threefold rotational symmetry around the out-of-plane [111] axis. The schematic illustrates the SHG experiment, with the polarizations of the fundamental and the second harmonic lights set to be parallel. b) Temperature-dependent Raman spectra of (111)-BTO. The characteristic Raman modes of BTO are labeled.

These results are therefore consistent with the inferred phase transitions in (111)-BTO from the dielectric spectra.

We further investigated the microscopic ferroelectric domain structure via STEM. Figure 3a shows a representative high-angle annular dark-field (HAADF)-STEM cross-sectional image of the (111)-BTO. The displacement vectors of the Ti cations with respect to the Ba cage are indicated by the overlaid arrows, which are proportional to the polarization of a unit cell.<sup>[37]</sup> As schematically illustrated in Figure 3b, the polar domains can be classified into Domains I, II, and III according to the polarization direction. Specifically, Domain I, with the Ti displacement vector projected along the [001] direction, can be assigned to either a tetragonal (displacing along [001]) or a rhombohedral (displacing along  $[\bar{1}11]$ ) phase. Domain II, showing the Ti displacement toward the edge of the Ba cage and rotating continuously from one side of the domain wall to the other, can be either orthorhombic (displacing around  $[\bar{1}01]$ ) or rhombohedra (displacing around  $[\bar{1}\bar{1}1]$ ) phase. Domain III, with the polarization projected along the  $[\bar{1}\bar{1}0]$  direction, can be considered as either an orthorhombic structure with  $[\bar{1}\bar{1}0]$  polarization or a tetragonal structure with  $[\bar{1}00]$  polarization. This result demonstrates phase coexistence in (111)-BTO at room temperature, as suggested by our Raman spectroscopy results.

The coexistence of different ferroelectric structures with varying symmetries provides considerable scope for polarization

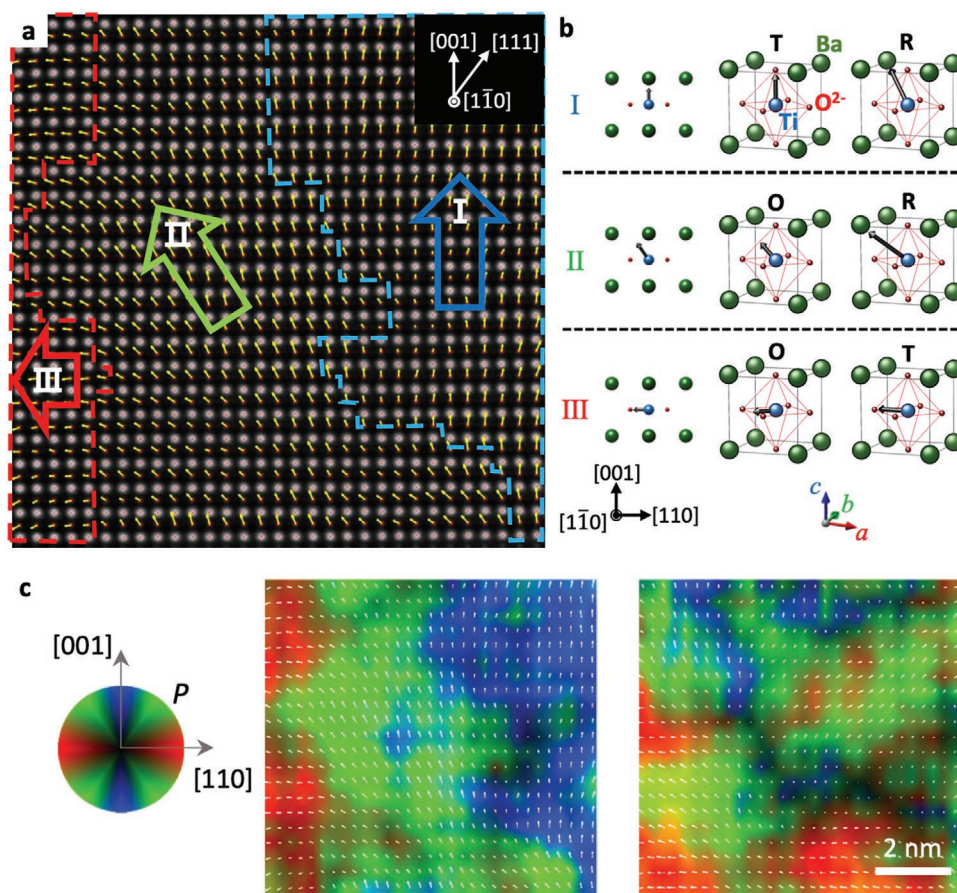


**Figure 3.** a) HAADF-STEM image of BTO in Pt/SRO/BTO/SRO/STO (111). Ti displacement vectors with respect to the Ba cage are indicated by the overlaid arrows. Domain I, II, and III, are classified according to the orientation of the Ti displacement vector. These domains are schematically illustrated in b), based on tetragonal (T), orthorhombic (O), and rhombohedral (R) structure models. c) 2D displacement vector mapping of the HAADF-STEM images acquired from different regions in the (111)-BTO film. The different hues (blue, green, and red) represent Domains I, II, and III, respectively. The brightness indicates the magnitude of the Ti displacement.

rotation via reduction of polarization anisotropy, which has a significant impact on the domain structure.<sup>[8,9,38,39]</sup> According to the aforementioned ferroelectric domains, we plotted the 2D polarization mappings of several STEM images acquired from different regions (Figure 3c and Figure S12, Supporting Information). All of the images indicate high-density nanodomains, with their sizes typically ranging from 1 to 10 nm. In particular, it is worth noting that, in all of the images, Domain II bridges the other two orthogonal polar domains (i.e., ferroelastic domains) via continuous polarization rotation. Such a bridging domain mechanism can significantly reduce the domain wall energy, thus inducing the observed domain miniaturization with high-density, low-angle domain walls.<sup>[39]</sup>

Phase-field simulation provides a way to further confirm the polymorphic nanodomain structure and, more importantly, elucidate the evolution of domains and phases in (111)-BTO with temperature. As a model system, we constructed a 20 nm thick BTO film with zero misfit strain (see the Experimental Section). Simulation results with varying misfit strain are compared in Figure S13 (Supporting Information). In line with our experimental observations, nanodomains with mixed tetragonal, orthorhombic, and rhombohedral structures form near room

temperature (Figure 4b). Moreover, the above-observed bridging domain configuration by means of polarization rotation is also verified. As the temperature decreases, large rhombohedral domains emerge while tetragonal and orthorhombic domains gradually disappear (Figure 4a). In contrast, at higher temperatures, the tetragonal phase begins to dominate (Figure 4c). The evolution of the phase volume fraction with temperature is shown in Figure 4d. In the temperature range near the dispersive dielectric relaxation peaks, namely 250 to 350 K, there is considerable phase instability to temperature fluctuations. This metastable state is a direct consequence of the complex local interaction involving local electrostatic as well as elastic forces, and the epitaxial constraint. Furthermore, a transition to a pure rhombohedral phase occurs at  $\approx 250$  K, again confirming the low-temperature phase transition event suggested by our dielectric analysis, Raman spectroscopy, and temperature-dependent SHG data (Figure S10, Supporting Information).

The simulation of ferroelectric domain structures under external electric fields offers a way to understand the remarkable dielectric and piezoelectric properties of (111)-BTO. As expected from the reduced polarization anisotropy in such a polymorphic nanodomain system, the simulation shows that

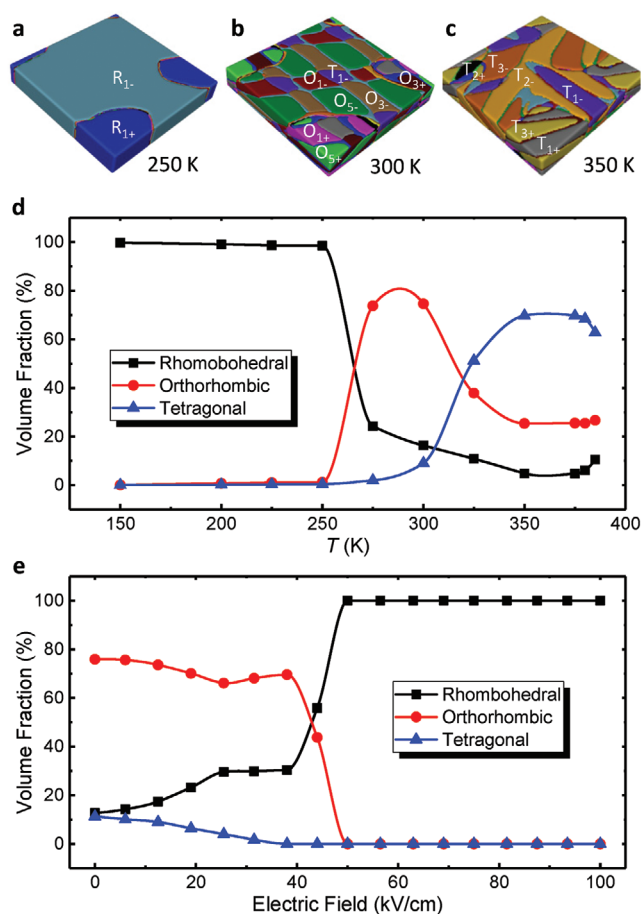


**Figure 4.** a–c) Phase-field simulations of (111)-BTO (20 nm thick) domain structures at a) 250 K, b) 300 K, and c) 350 K. Domain definitions:  $T_1: (\pm P_0, 0, 0)$ ,  $T_2: (0, \pm P_0, 0)$ ,  $T_3: (0, 0, \pm P_0)$ ,  $O_1: (\pm P_0, \pm P_0, 0)$ ,  $O_2: (\pm P_0, 0, \pm P_0)$ ,  $O_3: (0, \pm P_0, \pm P_0)$ , and  $R_1: (\pm P_0, \pm P_0, \pm P_0)$ . The lateral dimensions of the system are  $128 \times 128 \text{ nm}^2$ . The misfit strain of the film is assumed to be zero. d) The evolution of phase volume fractions with temperature. e) The evolution of phase volume fractions under electric bias applied along the out-of-plane direction.

the polarization in (111)-BTO is free to rotate toward the direction of the applied out-of-plane electric field, thus giving rise to an increasing volume fraction of rhombohedral domains (Figure 4e). Moreover, the coercive field for a complete phase transition is merely  $50 \text{ kV cm}^{-1}$ , corresponding to  $1.5 \text{ V}$  for a  $330 \text{ nm}$  thick film. Such a field-driven phase transition can explain the similar saturated out-of-plane polarizations in both (001)- and (111)-BTO (Figure 1b,c); otherwise the measured polarization in (111)-BTO would be only a fraction along the out-of-plane [111] direction of the titled polarization in tetragonal and orthorhombic variants. We can further infer that the polarization rotation is a continuous and smooth process, based on the absence of any discontinuous steps in the polarization switching of (111)-BTO (Figure 1c and Figure S6, Supporting Information). Interestingly, this scenario of field-driven polarization rotation and phase transition has indeed been reported in BTO bulk single crystals upon application of electric fields along the [111] direction.<sup>[40]</sup> This scenario also greatly enhanced  $d_{33}$  along the [111] direction. However, due

to the much bigger domain size and symmetry-restriction of a tetragonal structure in bulk BTO crystals, polarization rotation can only happen abruptly under a large critical electric field. Therefore, we believe this polarization-rotation scenario can be well established in the (111)-BTO, and could be a most plausible origin of the enhanced field-driven responses, as in other polymorphic nanodomain systems.<sup>[6,14,41]</sup>

### 3. Conclusion

In summary, we report a new polymorphic nanodomain system in a single-compound  $\text{BaTiO}_3$  film with optimized field-driven responses by epitaxial symmetry engineering. Notably, this concept can be widely applicable to epitaxy along other high-index orientations. In addition, the strategy does not rely on the misfit strain but a symmetry element of the mechanical constraint, which brings about a distinct advantage lying in its effectiveness in thick films, probably without a critical thickness as a common limiting parameter for traditional strain engineering. It is particularly interesting that the domain structure we observed in (111)-BTO resembles a slush-like polar structure of relaxor ferroelectrics with chemical inhomogeneities, thus giving rise to relaxor-like functional properties.<sup>[23]</sup> Therefore, our findings shed new lights on an avenue toward the development of on-chip devices using simple perovskite oxides as piezoelectric and dielectric elements.

### 4. Experimental Section

**Film Growth and Device Fabrication:** All the oxide films were grown on (001) or (111) STO substrates using a pulsed laser deposition (PLD) system with a KrF excimer laser (248 nm). A reflection high-pressure high-energy electron diffraction (RHEED) system was used to monitor the growth. Before deposition, STO substrates (miscut  $< 0.1^\circ$ ) were etched with a buffered hydrofluoric acid solution and then annealed in air at  $1000^\circ \text{C}$  for 3 h to produce atomically flat surface with unit-cell step terrace structure. It is especially important to note that (111) STO substrates need an additional pre-growth annealing process in the PLD chamber under ultrahigh vacuum ( $10^{-8} \text{ mTorr}$ ) at  $700^\circ \text{C}$  for 20 min to avoid surface degradation and reconstruction during growth (Figure S1, Supporting Information). During deposition, the temperature of the substrate was maintained at  $700^\circ \text{C}$  for the (001) case and  $670^\circ \text{C}$  for the (111) case. The SRO ultrathin films were grown under an oxygen pressure of 100 mTorr with a laser fluence of  $2 \text{ J cm}^{-2}$ . The BTO layers were subsequently deposited at an oxygen pressure of 20 mTorr with a laser fluence of  $1 \text{ J cm}^{-2}$ .<sup>[42]</sup> Capacitor devices with a sandwich structure, namely Pt/SRO/BTO/SRO/STO, were fabricated by further depositing another layer of 20 nm thick  $\text{SrRuO}_3$  on top of BTO for symmetric electrical contact. A layer of 100 nm thick Pt was then deposited by sputtering on top for better contact. Circular-shaped top electrodes with a diameter of  $200 \mu\text{m}$  were patterned by photolithography and ion milling.

**Electrical Measurement:** Electrical measurements, including  $P$ - $E$  hysteresis loop and dielectric permittivity measurement, were done on the capacitor devices with a BTO film thickness of 330 nm.  $P$ - $E$  hysteresis loop was measured with a TF analyzer 3000. Dielectric permittivity was measured with an impedance analyzer (Agilent 4294A). In both measurements, a cold head (RDK, Sumitomo) equipped with a Pfeiffer vacuum pump was used to provide a low-temperature environment (from 400 K down to 4 K). A hot plate covered with aluminum foil was used to provide a high-temperature environment (up to 573 K).

**PFM Measurements:** PFM were performed at room temperature using a commercial scanning probe microscope (Cypher, MFP-3D; Asylum Research) with Ir/Pt-coated AFM tips (PPP-EFM; Nanosensors), using the dual alternating current resonance tracing (DART) mode.

**Effective  $d_{33}$  Measurements:** Piezoelectric property was measured with a Polytec OFV-5000 LSV that was equipped with a vibrometer scanning head PSV-400. A sine-wave driving voltage with a specific amplitude and frequency was generated with a function generator. The out-of-plane vibration velocity and displacement was measured with the LSV based on Doppler effect. The effective piezoelectric coefficient  $d_{33}$  under the mechanical clamping condition from the substrate was then calculated from dividing the measured film dilation by the applied voltage.

**SHG Measurements:** Femtosecond laser light (Vitara-T; Coherent) with a wavelength of 800 nm, 80 MHz repetition rate, and 30 fs duration, was used as a fundamental light in both a grazing incidence geometry and a normal incidence geometry (see the Supporting Information). Half-wave plane and polarizer was utilized to tune the polarization of fundamental light and SHG light, respectively. The intensity of SHG light was monitored by using a photomultiplier tube.

**Raman Spectroscopy Measurements:** Horiba LabRAM Aramis equipped with a 473 nm Cobolt DPSS laser was used to collect the Raman spectra in the backscattering geometry with a microscope attachment. The laser power at room temperature under a  $10\times$  Olympus objective is 5.5 mW. Room temperature measurement was performed under a  $100\times$  Olympus objective with a numeric aperture (NA) of 0.9. Temperature-dependent measurement was performed under a  $50\times$  Olympus objective with a NA of 0.5 and in a Linkam 600 stage. Neither a polarizer nor an analyzer was employed in the measurement.

**Atomic-Resolution Imaging by STEM:**  $\text{Ti}^{4+}$ -atomic displacement analysis of the (111)-BTO thin film was performed using TEM. Cross-sectional TEM specimens were prepared by focused ion beam milling (Helios 650 FIB, FEI) and further thinned by focused Ar-ion milling (NanoMill 1040, Fischione). Atomic-resolution HAADF-STEM experiments were performed using a spherical aberration-corrected TEM (JEM-ARM 200F, JEOL Ltd, Japan) equipped with cold field emission gun operated at 200 kV. Before STEM experiments, TEM specimens were cleaned up with plasma cleaner to remove hydrocarbon and amorphous materials from the surface. Then the specimen was loaded 12 h earlier to minimize the drift. In order to minimize the scan distortion and enhance the signal-to-noise ratio, 20 frames of HAADF-STEM images were acquired sequentially with a short dwell time of 1  $\mu\text{s}$  per pixel and the image series were registered through cross-correlation between consecutive images. The images were processed by average background subtraction filter (ABSF) and low pass filter to minimize the background noise. The atomic positions were calculated by Gaussian fitting method with seven parameters of customized MATLAB script. For the accurate peak position finding, small size B-site atomic peaks were obtained after removing first fitted big size A-site atomic peaks.  $\text{Ti}^{4+}$ -Atomic displacement was measured compared to the center of two nearest neighbor  $\text{Ba}^{2+}$  and  $\text{Ti}^{0-}$  alternately mixed atomic column positions.

**Phase-Field Simulations:** The phase field method was utilized to model the evolution of the (111)-BTO films, where the polarization fields are obtained by solving the Allen–Cahn or Time-Dependent Ginzburg Landau (TDGL) equations

$$\frac{\partial P_i(\mathbf{r}, t)}{\partial t} = -L \frac{\delta F}{\delta P_i(\mathbf{r}, t)}, (i = 1, 2, 3) \quad (1)$$

where  $L$ ,  $\mathbf{r}$ , and  $t$  represent a kinetic coefficient relating to domain wall energy, spatial coordinates, and time, respectively. The polarization field is represented by  $P_i$  and  $F$  is the free energy functional. The free energy functional contains contributions from the elastic, chemical (bulk), gradient, and electrostatic energies

$$F = \int (f_{\text{Landau}} + f_{\text{gradient}} + f_{\text{electric}} + f_{\text{elastic}}) dV \quad (2)$$

An eighth order Landau–Ginzburg–Devonshire phenomenological potential was utilized to describe the Landau chemical energy, with

the expression coefficients used from Wang et al. and Li et al.<sup>[43,44]</sup> The exact expressions and solving methods of each energy contribution can be found in the literature.<sup>[45]</sup> The semi-implicit Fourier spectral method (SIFS) was utilized to solve the TDGL equations and evolve the domain structure.<sup>[46]</sup> To initiate the simulation, process a small random noise was applied to each of the spatial grid points. The system size was  $(128 \Delta x) \times (128 \Delta x) \times (34 \Delta x)$  where  $\Delta x = 1.0 \text{ nm}$  and  $\Delta x$  are represented in the real space dimensions. The thickness of the thin film was divided between substrate (10  $\Delta x$ ), film (20  $\Delta x$ ) and air (4  $\Delta x$ ). A general Euler Transformation matrix was utilized to transform the thin film coordinates from a local (001) orientation to the (111) orientation, by proper selection of Euler angles  $\phi$ ,  $\theta$ , and  $\psi$ .<sup>[47,48]</sup> The SIFS method was used to solve the TDGL equations in the local coordinates and then are rotated to (111) orientation

$$\begin{pmatrix} \cos\phi \cos\psi - \cos\theta \sin\phi \sin\psi & \cos\psi \sin\phi + \cos\theta \cos\phi \sin\psi & \sin\theta \sin\psi \\ -\cos\theta \cos\psi \sin\phi - \cos\phi \sin\psi & \cos\theta \cos\phi \cos\psi - \sin\phi \sin\psi & \cos\psi \sin\theta \\ \sin\theta \sin\phi & -\cos\phi \sin\theta & \cos\theta \end{pmatrix} \quad (3)$$

To understand how the domain structure changes under electric field, an electric field of up to  $10^5 \text{ V cm}^{-1}$  was applied on the thin film's top surface. All calculations were done under zero misfit strain ( $\epsilon_{11} = \epsilon_{22} = \epsilon_{12} = 0$ ). The temperatures of the systems were varied from 150–400 K, in 10–25 K increments to capture the phase transitions.

## Supporting Information

Supporting Information is available from the Wiley Online Library or from the author.

## Acknowledgements

J.A.Z. and J.M. contributed equally to this work. This work was supported by the Research Center Program of IBS (Institute for Basic Science) in Korea (IBS-R009-D1). STEM measurement was supported by the National Center for Inter-University Research Facilities (NCIRF) at Seoul National University in Korea. J.A.Z., B.W., and L.-Q.C. acknowledge the support by the Computational Materials Sciences Program funded by the US Department of Energy, Office of Science, Basic Energy Sciences, under Award Number DE-SC0020145 (J.A.Z. and L.-Q.C.) and by the US National Science Foundation under Award Number NSF-MRSEC DMR-1420620 (B.W.) and a fellowship from 3M Incorporated. Computations for this research were performed on the Pennsylvania State University's Institute for CyberScience Advanced CyberInfrastructure, and the Extreme Science and Engineering Discovery Environment (XSEDE) through NSF DMR170006. C.J.R. and J.S.L. acknowledge the support from Science Research Center and the Basic Science Research Program through the National Research Foundation of Korea (NRF) funded by the Ministry of Science, ICT & Future Planning (2018R1A2B2005331). The authors from IMRE acknowledge the supports by National Research Foundation Competitive Research Programme of Singapore, NRF-CRP15-2015-04, (IMRE/16-9P1122). M.S., C.W.A., and T.H.K. acknowledge the support from the Priority Research Centers Program through the National Research Foundation of Korea (NRF) funded by the Ministry of Education (Grant No. NRF-2019R1A6A1A11053838). The authors acknowledge invaluable suggestions and support from S. M. Yang, Z.-G. Ye, S. H. Chang, and J. H. Ko.

## Conflict of Interest

The authors declare no conflict of interest.

## Keywords

dielectric, epitaxial films, oxide ferroelectrics, piezoelectric, polymorphic nanodomains

Received: December 19, 2019

Revised: January 30, 2020

Published online: February 24, 2020

- [1] X. Ren, K. Otsuka, *Nature* **1997**, 389, 579.
- [2] A. Moreo, S. Yunoki, E. J. S. Dagotto, *Science* **1999**, 283, 2034.
- [3] F. Li, D. Lin, Z. Chen, Z. Cheng, J. Wang, C. Li, Z. Xu, Q. Huang, X. Liao, L.-Q. Chen, T. R. Shrout, S. Zhang, *Nat. Mater.* **2018**, 17, 349.
- [4] R. Zeches, M. Rossell, J. Zhang, A. Hatt, Q. He, C.-H. Yang, A. Kumar, C. Wang, A. Melville, C. Adamo, *Science* **2009**, 326, 977.
- [5] M. Ahart, M. Somayazulu, R. E. Cohen, P. Ganesh, P. Dera, H.-k. Mao, R. J. Hemley, Y. Ren, P. Liermann, Z. Wu, *Nature* **2008**, 457, 545.
- [6] B. Noheda, D. E. Cox, G. Shirane, J. A. Gonzalo, L. E. Cross, S.-E. Park, *Appl. Phys. Lett.* **1999**, 74, 2059.
- [7] G. A. Rossetti Jr., A. G. Khachatryan, *Appl. Phys. Lett.* **2007**, 91, 072909.
- [8] J. Gao, X. Hu, Y. Liu, Y. Wang, X. Ke, D. Wang, L. Zhong, X. Ren, *J. Phys. Chem. C* **2017**, 121, 2243.
- [9] G. A. Rossetti Jr., A. G. Khachatryan, G. Akcay, Y. Ni, *J. Appl. Phys.* **2008**, 103, 114113.
- [10] K. A. Schönau, L. A. Schmitt, M. Knapp, H. Fuess, R.-A. Eichel, H. Kungl, M. J. Hoffmann, *Phys. Rev. B* **2007**, 75, 184117.
- [11] H. Wu, Y. Zhang, J. Wu, J. Wang, S. J. Pennycook, *Adv. Funct. Mater.* **2019**, 29, 1902911.
- [12] F. Li, S. Zhang, D. Damjanovic, L.-Q. Chen, T. R. Shrout, *Adv. Funct. Mater.* **2018**, 28, 1801504.
- [13] A. R. Damodaran, S. Pandya, J. C. Agar, Y. Cao, R. K. Vasudevan, R. Xu, S. Saremi, Q. Li, J. Kim, M. R. McCarter, L. R. Dedon, T. Angsten, N. Balke, S. Jesse, M. Asta, S. V. Kalinin, L. W. Martin, *Adv. Mater.* **2017**, 29, 1702069.
- [14] J. X. Zhang, B. Xiang, Q. He, J. Seidel, R. J. Zeches, P. Yu, S. Y. Yang, C. H. Wang, Y. H. Chu, L. W. Martin, A. M. Minor, R. Ramesh, *Nat. Nanotechnol.* **2011**, 6, 98.
- [15] A. S. Everhardt, S. Matzen, N. Domingo, G. Catalan, B. Noheda, *Adv. Electron. Mater.* **2016**, 2, 1500214.
- [16] R. D. Anoop, C. A. Joshua, P. Shishir, C. Zuhuang, D. Liv, X. Ruijuan, A. Brent, S. Sahar, W. M. Lane, *J. Phys.: Condens. Matter* **2016**, 28, 263001.
- [17] Y. Tang, Y. Zhu, X. Ma, Z. Hong, Y. Wang, W. Wang, Y. Xu, Y. Liu, B. Wu, L. Chen, C. Huang, L. Chen, Z. Chen, H. Wu, S. J. Pennycook, *Adv. Funct. Mater.* **2019**, 29, 1901687.
- [18] R. Xu, S. Liu, S. Saremi, R. Gao, J. J. Wang, Z. Hong, H. Lu, A. Ghosh, S. Pandya, E. Bonturim, Z.H. Chen, L.Q. Chen, A.M. Rappe, L.W. Martin, *Nat. Commun.* **2019**, 10, 1282.
- [19] R. Xu, S. Liu, I. Grinberg, J. Karthik, A. R. Damodaran, A. M. Rappe, L. W. Martin, *Nat. Mater.* **2015**, 14, 79.
- [20] R. E. Cohen, *Nature* **1992**, 358, 136.
- [21] S. Kobayashi, K. Inoue, T. Kato, Y. Ikuhara, T. Yamamoto, *J. Appl. Phys.* **2018**, 123, 064102.
- [22] G. Sheng, J. X. Zhang, Y. L. Li, S. Choudhury, Q. X. Jia, Z. K. Liu, L. Q. Chen, *Appl. Phys. Lett.* **2008**, 93, 232904.
- [23] H. Takenaka, I. Grinberg, S. Liu, A. M. Rappe, *Nature* **2017**, 546, 391.
- [24] D. Fu, H. Taniguchi, M. Itoh, S.-Y. Koshihara, N. Yamamoto, S. Mori, *Phys. Rev. Lett.* **2009**, 103, 207601.
- [25] H. Pan, J. Ma, J. Ma, Q. Zhang, X. Liu, B. Guan, L. Gu, X. Zhang, Y.-J. Zhang, L. Li, Y. Shen, Y.-H. Lin, C.-W. Nan, *Nat. Commun.* **2018**, 9, 1813.
- [26] S. Shetty, A. Damodaran, K. Wang, Y. Yuan, V. Gopalan, L. Martin, S. Trolier-McKinstry, *Adv. Funct. Mater.* **2019**, 29, 1804258.
- [27] R. Xu, J. Karthik, A. R. Damodaran, L. W. Martin, *Nat. Commun.* **2014**, 5, 3120.
- [28] A. A. Bokov, Z.-G. Ye, *J. Adv. Dielectr.* **2012**, 02, 1241010.
- [29] K. A. Schönau, M. Knapp, M. Maglione, H. Fuess, *Appl. Phys. Lett.* **2009**, 94, 122902.
- [30] D. Sheen, J.-J. Kim, *Phys. Rev. B* **2003**, 67, 144102.
- [31] K. Yao, F. E. H. Tay, *IEEE Trans. Ultrason. Ferroelectr. Freq. Control.* **2003**, 50, 113.
- [32] S. Kumar, D. Kumar, V. G. Sathe, R. Kumar, T. K. Sharma, *J. Appl. Phys.* **2015**, 117, 134103.
- [33] Y. Shiratori, C. Pithan, J. Dornseiffer, R. Waser, *J. Raman Spectrosc.* **2007**, 38, 1300.
- [34] N de Mathan, E. Husson, G. Calvarin, J. R. Gavarri, S. W. Hewat, A. Morell, *J. Phys.: Condens. Matter* **1991**, 3, 8159.
- [35] Y. M. Jin, Y. U. Wang, A. G. Khachatryan, J. F. Li, D. Viehland, *J. Appl. Phys.* **2003**, 94, 3629.
- [36] D. A. Tenne, X.X. Xi, Y. L. Li, L. Q. Chen, A. Soukiassian, M. H. Zhu, A. R. James, J. Lettieri, D. G. Schlom, W. Tian, X. Q. Pan, *Phys. Rev. B* **2004**, 69, 174101.
- [37] G. H. Kwei, A. C. Lawson, S. J. L. Billinge, S. W. Cheong, *J. Phys. Chem.* **1993**, 97, 2368.
- [38] Y. M. Jin, Y. U. Wang, A. G. Khachatryan, J. F. Li, D. Viehland, *Phys. Rev. Lett.* **2003**, 91, 197601.
- [39] W.-F. Rao, Y. U. Wang, *Appl. Phys. Lett.* **2007**, 90, 182906.
- [40] S. Wada, S. Suzuki, T. Noma, T. Suzuki, M. Osada, M. Kakihana, S.-E. Park, E. Cross, T. R. Shrout, *Jpn. J. Appl. Phys.* **1999**, 38, 5505.
- [41] F. Li, S. Zhang, T. Yang, Z. Xu, N. Zhang, G. Liu, J. Wang, J. Wang, Z. Cheng, Z.-G. Ye, J. Luo, T. R. Shrout, L.-Q. Chen, *Nat. Commun.* **2016**, 7, 13807.
- [42] Y. J. Shin, Y. Kim, S.-J. Kang, H.-H. Nahm, P. Murugavel, J. R. Kim, M. R. Cho, L. Wang, S. M. Yang, J.-G. Yoon, J.-S. Chung, M. Kim, H. Zhou, S. H. Chang, T. W. Noh, *Adv. Mater.* **2017**, 29, 1602795.
- [43] Y. L. Li, L. E. Cross, L. Q. Chen, *J. Appl. Phys.* **2005**, 98, 064101.
- [44] J. J. Wang, F. Y. Meng, X. Q. Ma, M. X. Xu, L. Q. Chen, *J. Appl. Phys.* **2010**, 108, 034107.
- [45] Y. L. Li, S. Y. Hu, Z. K. Liu, L. Q. Chen, *Acta Mater.* **2002**, 50, 395.
- [46] L. Q. Chen, J. Shen, *Comput. Phys. Commun.* **1998**, 108, 147.
- [47] R. E. Newnham, *Properties of Materials: Anisotropy, Symmetry, Structure*, Oxford University Press, UK **2005**.
- [48] S. Choudhury, Y. Li, C. Krill III, L.-Q. Chen, *Acta Mater.* **2005**, 53, 5313.